

The Structure and Properties of Amorphous Indium Oxide

D. Bruce Buchholz,[†] Qing Ma,[‡] Diego Alducin,[◇] Arturo Ponce,[◇] Miguel Jose-Yacamán,[◇] Rabi Khanal,[#] Julia E. Medvedeva,[#] Robert P.H. Chang[†]

[†]Department of Materials Science and Engineering, Northwestern University, Evanston, IL 60208

DND-CAT, Northwestern Synchrotron Research Center at the Advanced Photon Source, Argonne National Laboratory, Argonne, IL 60439

[◇]Department of Physics and Astronomy, University of Texas at San Antonio, San Antonio, TX 78249

[#]Department of Physics Missouri University of Science & Technology, Rolla, MO 65409-0640

SUPPORTING INFORMATION

SURVEY OF PRIOR EXAFS STUDIES

D. Proffitt, et al., investigated the In, Sn and Zn k-edges of 250 nm thick amorphous $\text{Zn}_{0.3}\text{In}_{1.4}\text{Sn}_{0.3}\text{O}_7$ (*a*-ZITO), thin films deposited on SiO_2 glass by pulsed laser deposition.¹ This study looks at first-shell bonding. The values of σ^2 reported in table 1 are an average. Hoel, et al., investigated the In, Sn and Zn k-edges of powder $\text{Zn}_{0.3}\text{In}_{1.4}\text{Sn}_{0.3}\text{O}_7$ (*a*-ZITO) samples.² In order to gain second-shell bonding information, because of the complexity of the structure, several constraints had to be imposed in fitting the data. Among these were: In the first shell $N_{\text{In-O}}$ and $N_{\text{Zn-O}}$ were both fixed at 6; in the second shell when looking at *In-M* and *Sn-M* only In was considered as the nearest neighbor (*M*) and the total number of *In-In* neighbors was set at 12. The first-shell information is in table 1. A main conclusion of this data is that the zinc is tetrahedrally coordinated. D-Y. Cho, et al., investigated the In, Ga, Zn and O k-edges of 150 nm thick *a*-IGZO thin films deposited on SiO_2 glass by rf-sputtering.³ Two compositions of IGZO were examined; InGaZnO_4 (1114) and $\text{In}_2\text{Ga}_2\text{ZnO}_7$ (2217). In their analysis they were able to differentiate two values for $R_{\text{Zn-O}}$ and hence two values for $N_{\text{Zn-O}}$. The Fourier transform for magnitudes at $R > 3 \text{ \AA}$ were suppressed such that only data for the first shell could be obtained. K. Nomura, et al., investigated the In, Ga, and Zn k-edges of 250 nm thick *a*-IGZO thin films, InGaZnO_4 (1114), deposited on SiO_2 glass by pulsed laser deposition.⁴ D-S. Yang, et al., investigated the In, Zn, Ga and Hf k-edges of 40 nm thick films deposited on glass by rf-sputtering of: *a*-IGZO, In:Ga:Zn of

33:33:33 (1114); *a*-IHZO, In:Hf:Zn of 35:10:55; and *a*-IZO, In:Zn of 45:45[*sic*].⁵ F. Utsuno, et al., investigated both the In and Zn k-edges of 500 nm thick *a*-IZO thin films deposited on fused quartz by rf-sputtering.⁶ They looked at three Zn concentrations 6.1%, 10.7% and 37.0%. T. Moriga, et al., investigated 150 nm thick IZO, Zn₅In₂O₈, thin films by the sol-gel method.⁷ At low firing temperatures x-ray diffraction patterns revealed only wurtzite-type ZnO; the In₂O₃ was therefore assumed to be amorphous. EXAFS was used to probe the In k-edge of materials believed to an amorphous indium oxide (*a*-IO) phase.

Material	ZITO ¹	ZITO ²	IGZO ³	IGZO ³	IGZO ⁶	IGZO ⁵	IHZO ⁵	IZO ⁵	IZO ⁶	IZO ⁷
			2217	1114	1114	1114				
N_{In-O}	5.0	6 (set)	6.1	5.8	4.5	5.3	5.9	5.8	6.0	4.9-5.0
$R_{In-O}(\text{Å})$	2.14	2.140	2.24	2.30	2.11	2.13	2.13	2.14	-	~2.1
$\sigma^2_{In-O}(\text{Å})^2$	0.008	0.0083	0.005	0.005	0.0077	0.00068	0.0007	0.0007	-	0.01*
N_{Zn-O}	3.3	~4	2.5	2.5	4.6	3.2	3.4	3.5	4.0	-
$R_{Zn-O}(\text{Å})$	1.98	1.97	1.91	1.91	1.95	1.98	1.98	1.97	-	-
$\sigma^2_{Zn-O}(\text{Å})^2$	0.007	-	0.005	0.005	0.0081	0.00076	0.0006	0.0006	-	-
N_{Sn-O}	-	-	2.3	2.0	-	-	-	-	-	-
$R_{Sn-O}(\text{Å})$	-	-	2.10	2.10	-	-	-	-	-	-
$\sigma^2_{Sn-O}(\text{Å})^2$			0.005	0.005	-			-	-	-
N_{Ga-O}	5.9	6 (set)	-	-	-	-	-	-	-	-
$R_{Ga-O}(\text{Å})$	2.07	2.058	-	-	-	-	-	-	-	-
$\sigma^2_{Ga-O}(\text{Å})^2$	0.006	0.0045	-	-	-	-	-	-	-	-
N_{Hf-O}	-	-	4.8	4.9	4.3	6.4	-	-	-	-
$R_{Hf-O}(\text{Å})$	-	-	1.91	1.93	2.00	1.87	-	-	-	-
$\sigma^2_{Hf-O}(\text{Å})^2$			0.005	0.005	0.0067	0.0006	-	-	-	-
N_{Hf-O}	-	-	-	-	-	-	6.8	-	-	-
$R_{Hf-O}(\text{Å})$	-	-	-	-	-	-	2.06	-	-	-
$\sigma^2_{Hf-O}(\text{Å})^2$	-	-	-	-	-	-	0.0003	-	-	-

Table S1: First shell structure of indium based *a*-TCOs and *a*-TOSs; * value obtained by squaring reported σ .

EXAFS ANALYSIS

The rationale by which the analysis parameters for the modeling of the extended x-ray analysis fine structure (EXAFS) data are chosen, although not of interest to all, is worthy of documentation and done so in this section. In crystalline In₂O₃ (*c*-IO), figure S1, the oxygen atoms are octahedrally coordinated around indium; all indium cations are surrounded by 6 oxygen atoms ($c-N_{InO} = 6$) at an average distance of 2.18 Å ($c-R_{InO} = 2.18$ Å) as well as 2 structural vacancies; this is the first-shell. The existence of structural vacancies gives rise to two

configurations by which, in *c*-IO, the InO_6 octahedra link together: In the first, two oxygen are shared between the adjacent polyhedra with the end result that the polyhedral are joined along the entire edge and hence are called “edge sharing”; in the second, both an oxygen and a structural vacancy are shared between adjacent polyhedra with the end result that the polyhedral are only joined at a corner and hence they are called “corner sharing”, figure S1. This leads to two distinct sets of adjacent InO_6 polyhedra *In-In* neighbors: There are six-adjacent edge-sharing polyhedra ($N_{\text{In-In}} = 6$) at a distance of $\sim 3.3 \text{ \AA}$ ($R_{\text{In-In}} = 3.3 \text{ \AA}$) and six-adjacent corner-sharing polyhedra ($N_{\text{In-In}^*} = 6$) at a distance of $\sim 3.8 \text{ \AA}$ ($R_{\text{In-In}^*} = 3.8 \text{ \AA}$); these make up the second and third-shell around indium respectively.

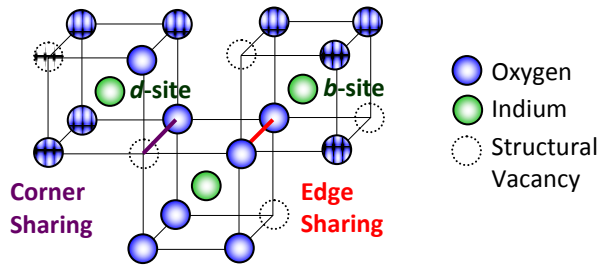


Figure S1: Structure of crystalline In_2O_3 (bixbyite)

The analysis is done within the context of the ARTEMAS software package.⁸ When data is fit to a single-shell (first shell) model, the following parameters can either be set to a fixed-value or have a derived-value determined by the fit:

S_0^2 , an amplitude factor that aligns the magnitude of the experimental data with the software derived model.

ΔE_0 , an “alignment offset energy” used within the contest of first shell to align the data with respect to the theoretical calculations within the model.

$N_{\text{In-O}}$, the first shell *In-O* coordination number.

$R_{\text{In-O}}$, the first shell *In-O* bond distance.

$\sigma_{\text{In-O}}^2$, the first shell statistical spread in the *In-O* bond distance.

When data is fit to a three-shell (first, second and third shell) model, in addition to the parameters listed above the following additional parameters can either be set to a fixed-value or have a derived-value determined by the fit:

$\Delta E_0'$, an “alignment offset energy” used within the context of second and third-shells to align the data with respect to the theoretical calculations within the model. A charge imbalance in the FEFF calculations within ARTEMAS of the first atomic potentials with respect to all other potential can result in the need for a separate ΔE for the first shell.⁹

N_{In-In} and N_{In-In^*} , the second and third shell *In-In* coordination numbers respectively.

R_{In-In} and R_{In-In^*} , the second and third shell *In-In* bond distances respectively.

σ^2_{In-In} and $\sigma^2_{In-In^*}$, the second and third shell statistical spread in the *In-In* bond distances respectively.

Herein is the rationale by which S_0^2 , *R*-range, *k*-range, and ΔE values were chosen for in the analysis of the EXAFS within the context of the ARTEMAS software package.

Choice of *k*-range

The choice of values is complicated by the fact that both amorphous and highly crystalline samples are analyzed. The *k*-space plot in figure S2a is for In_2O_3 (IO) deposited at 600°C that is highly crystalline (*c*-IO). Oscillations are clearly visible to greater than 15.5 \AA^{-1} .

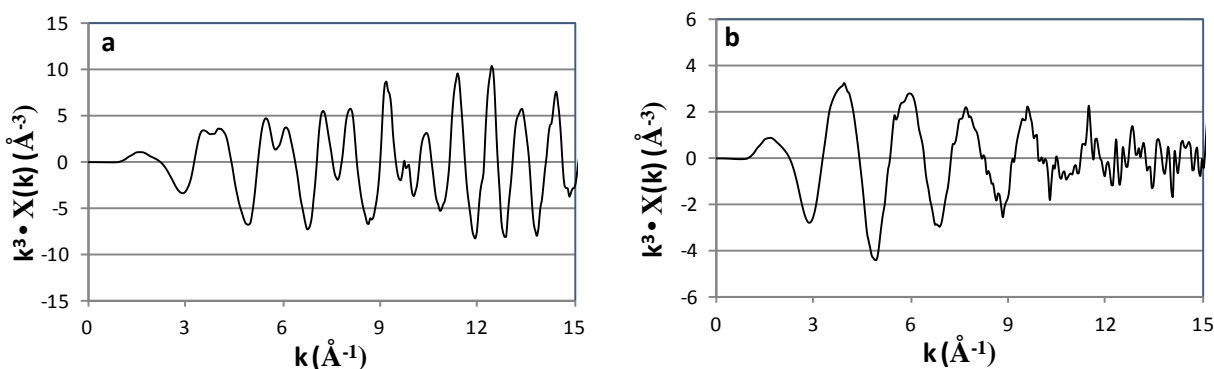


Figure S2: a) Highly crystalline IO deposited at 600°C b) amorphous IO deposited at 0°C.

Figure S2b is for an amorphous IO (*a*-IO); here clear oscillations only extend to $\sim 10 \text{ \AA}^{-1}$ with discernible oscillations to $\sim 13 \text{ \AA}^{-1}$. Use of a k -range $> 13 \text{ \AA}^{-1}$ for the amorphous samples would add mostly noise. In both cases the oscillations start at $\sim 2.24 \text{ \AA}^{-1}$. Therefore, for the comparative analysis of both *c*-IO and *a*-IO a k -range of 2.24 \AA^{-1} to $\sim 13 \text{ \AA}^{-1}$ will be use. The effects of limiting the k -range will be examined further later in this text.

Choice of R -range

The choice of the R -range will depend on how many shells are included in the fit. Looking at the Fourier transform of a crystalline In_2O_3 powder standard, $0 < k < 16 \text{ \AA}^{-1}$ and a k -weight (kw) of 3, figure S3a, the approximate bounds appear to be $\sim 2.0 \text{ \AA}$ for the first shell, $\sim 3.3 \text{ \AA}$ for the second shell and $\sim 4 \text{ \AA}$ for the third shell. There is, however, shown in figure S3b were the contributions to the Fourier transform are broken out by shell, considerable overlap between the second and third shell. The apparently clear demarcation between the second and third shells at $\sim 3.3 \text{ \AA}$ in figure S3a is a destructive interference effect in k -space and can be seen in the when looking at the real part (or imaginary part) of the Fourier transform, Figure S3c. The autonomy of the first shell is still evident in figure S3b and S3c, hence, for single-shell fitting of the first shell a R -range of $\sim 1 \text{ \AA} \leq R \leq \sim 2 \text{ \AA}$ will be used. For multiple-shell fitting, if only the first two shells are included in the fit, the truncation of the second shell and the overlap of the third shell may introduce error. Therefore, the first three-shells will be used in multiple-shell (three-shell) fitting and an R -range of $\sim 1 \text{ \AA} \leq R \leq \sim 4 \text{ \AA}$ will be used.

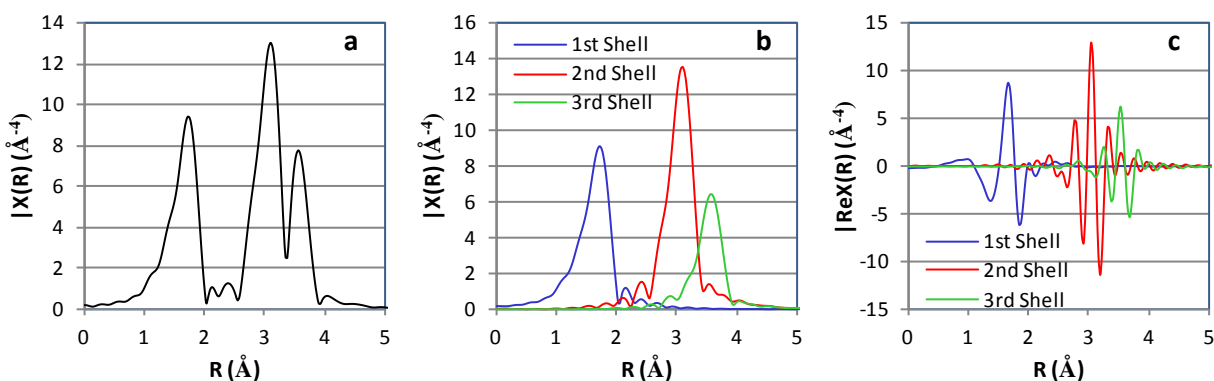


Figure S3: a) Radial distribution for *c*-IO powder standard. b) Magnitude of Fourier contributions from 1st-shell (blue), 2nd-shell (red) and 3rd-shell (green). c) Real part of Fourier contributions from 1st-shell (blue), 2nd-shell (red) and 3rd-shell (green).

Choice of S_0^2

For the determination of S_0^2 the powdered In_2O_3 standard was used and assumed (set) to have $N_{\text{In-O}} = 6$, $N_{\text{In-In}} = 6$ and $N_{\text{In-In}^*} = 6$. A k -weight (kw) of 2 was used. (A $kw = 2$ was chosen for all analysis as experience revealed it to provide more stable results with respect to small changes of R -range and k -range.) This, as well as all subsequent fits, was done in R -space. Because the powdered In_2O_3 standard was used, the k -range could span the entire data range of $2.24 \text{ \AA}^{-1} < k < 14.64 \text{ \AA}^{-1}$; the last complete oscillation in k -space occurred at 14.64 \AA^{-1} . The values of ΔE , $R_{\text{In-O}}$, $\sigma_{\text{In-O}}^2$ and S_0^2 were allowed to vary and be fit by the ARTEMIS software. For the single-shell model a R -range of $1 \text{ \AA} \leq R \leq 2 \text{ \AA}$ was used and a value of $S_0^2 = 1.02 (\pm 0.04)$ obtained. For the three-shell model a R -range of $1 \text{ \AA} \leq R \leq 4 \text{ \AA}$ was used and a value of $S_0^2 = 1.03 (\pm 0.03)$ obtained. In both the single-shell and three-shell fits the values for the other fit parameters, ΔE , $R_{\text{In-O}}$ and $\sigma_{\text{In-O}}^2$, were highly reasonable and as might be expected for crystalline In_2O_3 .

Choice of ΔE_0

Limiting the k -range can affect the fit. To ensure a reliable value of ΔE_0 was obtained the effect of limiting the k -range on ΔE_0 for the powdered c -IO standard and the a -IO sample deposited at 0°C was examined. The single-shell model was used: $S_0^2 = 1.02$ was set; ΔE_0 , $N_{\text{In-O}}$, $R_{\text{In-O}}$ and $\sigma_{\text{In-O}}^2$ determined by the model fit; $kw = 2$; $1 \text{ \AA} \leq R \leq 2 \text{ \AA}$; the lower limit to the k -range, k_{min} , was 2.24 \AA^{-1} , for reasons enumerated earlier; the upper limit of the k -range, k_{max} , assumed the values of 9.49 \AA^{-1} , 10.0 \AA^{-1} , 10.63 \AA^{-1} , 11.0 \AA^{-1} , 11.63 \AA^{-1} , 12.0 \AA^{-1} , 12.67 \AA^{-1} , 13.2 \AA^{-1} , 13.61 \AA^{-1} and 14.64 \AA^{-1} as these were points that corresponded to where the data for either the c -IO standard or a -IO sample completed a cycle k -space. As can be seen in figures S4a and b the choice of k_{max} has very little effect on ΔE_0 . Therefore, for any deposition temperature, the value

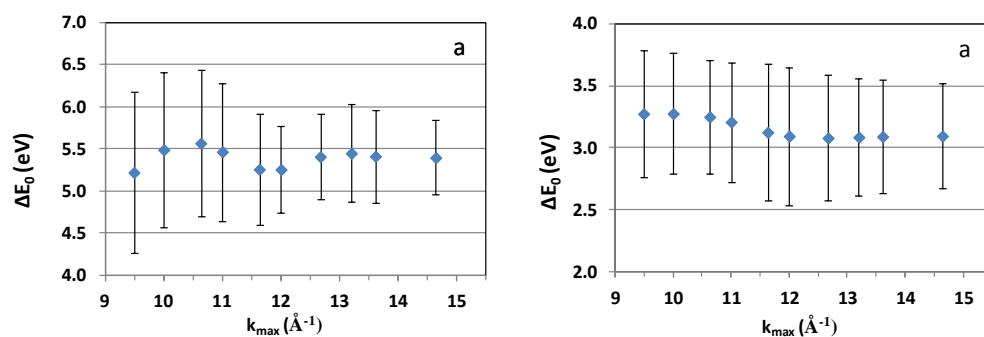


Figure S4: ΔE_0 as a function of k_{max} for a) c -IO powder standard, b) 0°C amorphous sample.

of ΔE_0 will be determined with a $k_{max} = 12.67 \text{ \AA}^{-1}$, the largest value of k for which a completed cycle in k -space occurs above the noise level for all temperatures. The large uncertainty in the value of ΔE_0 (the error bars) is due to the fact that both ΔE_0 and R_{In-O} , were allowed to vary during the fit; these two variables are correlated. If the value of one of the variables is fixed then the uncertainty of the other decreases dramatically. In summary, for each deposition temperature the value of ΔE_0 will be determined using the single (first) shell model, a R -range of $\sim 1 \text{ \AA} \leq R \leq \sim 2 \text{ \AA}$, a k -range $2.24 \text{ \AA}^{-1} \leq k \leq 12.67 \text{ \AA}^{-1}$ and a $k_w = 2$.

At the same time the values of ΔE_0 as a function of k_{max} for the c -IO standard and the a -IO sample were determined, values for N_{In-O} , R_{In-O} , and σ^2_{In-O} were also obtained, figures S5a-f. They are worth mentioning if only for later comparison to the values obtained in the three-shell model. Again, the values obtained are largely independent of k_{max} although a small effect can be observed for $k_{max} < \sim 11 \text{ \AA}^{-1}$. Fortunately, our choice of $k_{max} = 12.67 \text{ \AA}^{-1}$ renders this point moot for these studies. With the value of ΔE_0 set, the value of $\Delta E_0'$ can now be determined.

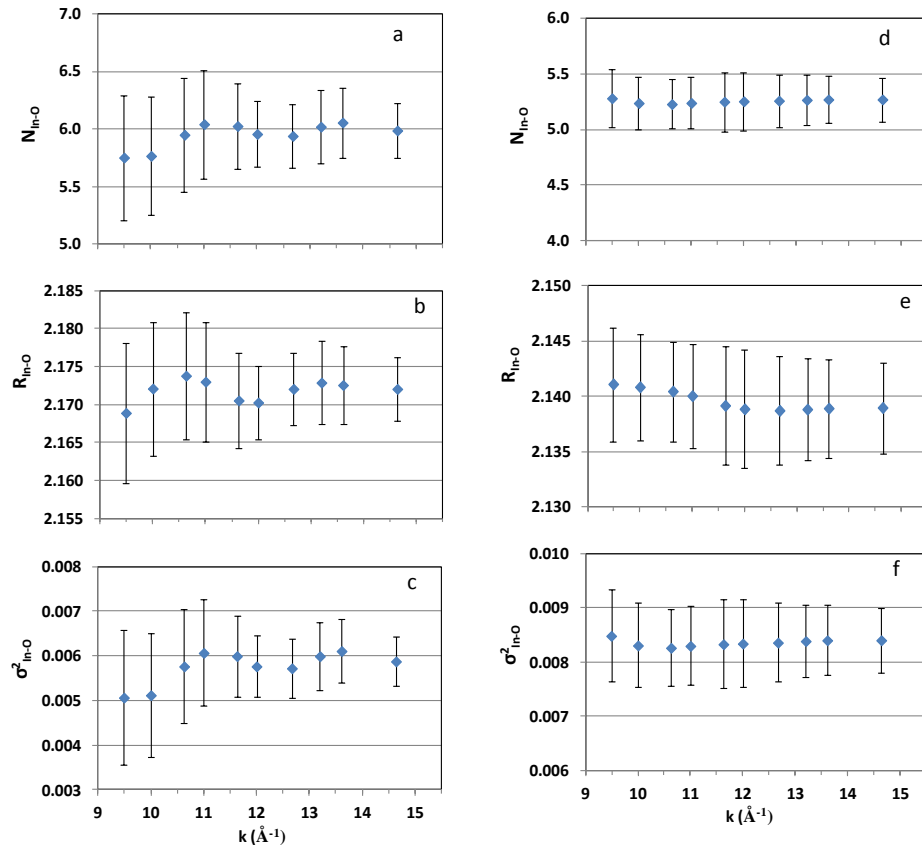


Figure S5: For the powder c -IO standard a) N_{In-O} , b) R_{In-O} , and c) σ^2_{In-O} , as a function of k_{max} ; for the 0°C amorphous sample d) N_{In-O} , e) R_{In-O} , and f) σ^2_{In-O} , as a function of k_{max} .

Choice of $\Delta E_0'$

To determine the “alignment energy offset” for the second and third shells, $\Delta E_0'$, the three-shell model was used: $S_0^2 = 1.03$ was set; ΔE_0 was determined from the single-shell model as described above and set prior to three-shell fitting; $\Delta E_0'$, N_{In-O} , R_{In-O} , σ_{In-O}^2 , N_{In-In} , R_{In-In} , σ_{In-In}^2 , N_{In-In*} , R_{In-In*} and σ_{In-In*}^2 were allowed to vary and determined by the model fit; $k_W = 2$; $1 \text{ \AA} \leq R \leq 4 \text{ \AA}$; $k_{min} = 2.24 \text{ \AA}^{-1}$, k_{max} the same as for the determination of ΔE_0 . Unlike the determination of ΔE_0 with a single shell model, figure S4a, $\Delta E_0'$ is affected by the choice of k -range, figure S6. A

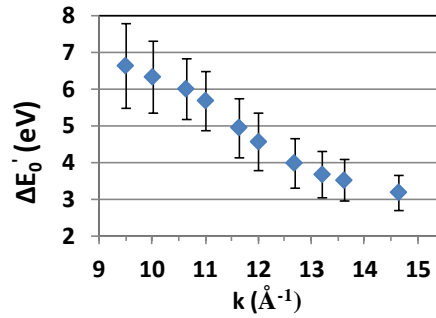


Figure S6: $\Delta E_0'$ as a function of k_{max} for the *c*-IO powder standard.

portion of the information used to align the theoretical model with the experimental data for the second and third shell is contained in the higher k -range, this is true to a much lesser extent for the first shell, figure S7. The effect of limiting the k -range can also be seen by looking at the

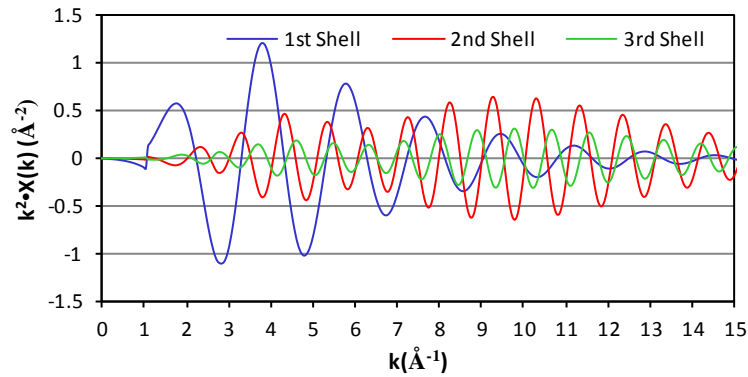


Figure S7: $k^2 \cdot X(k)$ as a function of k_{max} for the *c*-IO powder standard.

values of N_{In-In} , R_{In-In} , σ_{In-In}^2 , N_{In-In*} , R_{In-In*} and σ_{In-In*}^2 as a function of k_{max} , figures S8d-i. Before looking at the second and third shell, it is worth noting that the values for N_{In-O} , R_{In-O} and σ_{In-O}^2 from the three-shell fit, figures S8a-c; they are essentially the same as the values from the single-shell fit, figures S5a-c; values as a function of k_{max} are more stable for the three-shell fit because ΔE_0 is fixed. Returning to the second and third shells, it can be seen that the values of R_{In-In} and R_{In-In*} are also a function of k_{max} . $\Delta E_0'$, R_{In-In} and R_{In-In*} , however, are not completely independent

but correlated. The correlation, however, can be separated given a sufficiently large set of data.

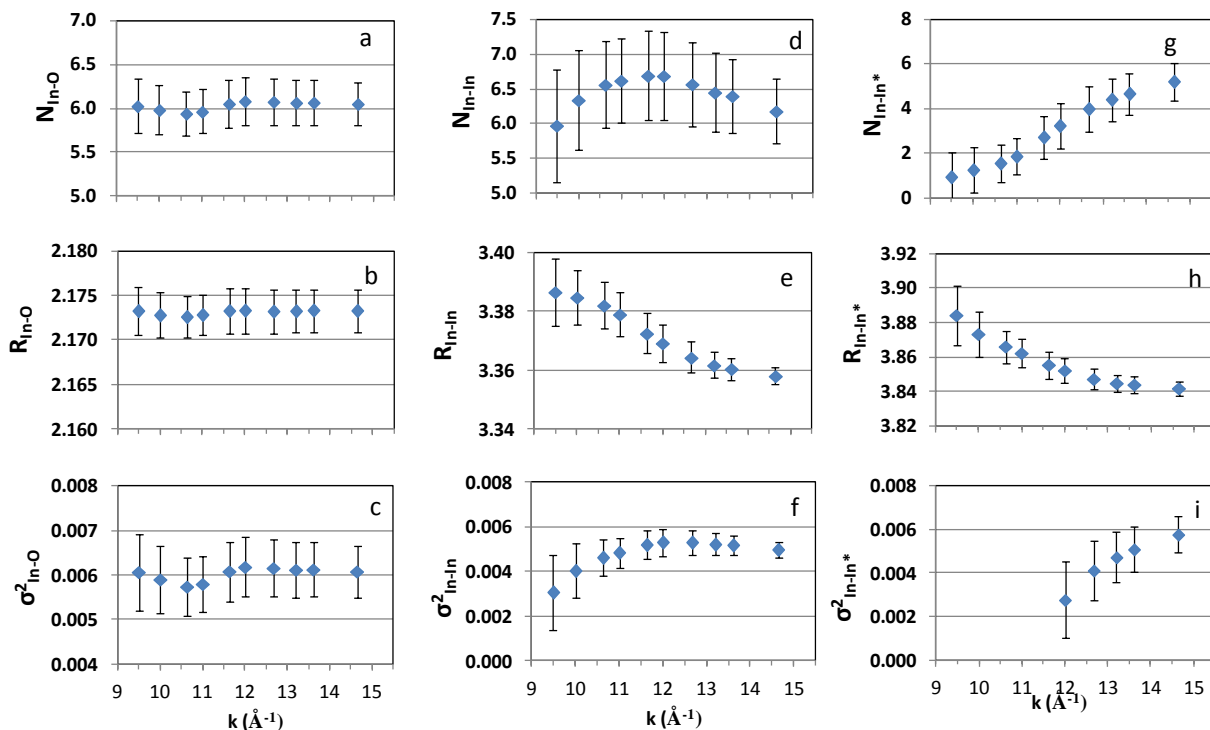


Figure S8: a) N_{In-O} , b) R_{In-O} , c) σ^2_{In-O} , d) N_{In-In} , e) R_{In-In} , f) σ^2_{In-In} , g) N_{In-In^*} , h) R_{In-In^*} , and i) $\sigma^2_{In-In^*}$ for the powder *c*-IO standard as a function of k_{max} ; $\Delta E_0'$ fit by model as a function of k_{max} .

Because there is a highly crystalline sample, where the usable k -range extends to $> 15 \text{ \AA}^{-1}$, we can assume the most accurate values are obtained for $k_{max} = 14.64 \text{ \AA}^{-1}$. This assumption is substantiated by the fact that the values for N_{In-In} , R_{In-In} , σ^2_{In-In} , N_{In-In^*} , R_{In-In^*} and $\sigma^2_{In-In^*}$ obtained for $k_{max} = 14.64 \text{ \AA}^{-1}$ are the most consistent with those expected for *c*-IO. Performing the analysis again but this time with $\Delta E_0'$ set to the value obtained at $k_{max} = 14.64 \text{ \AA}^{-1}$, and allowing all other variables to be fixed or varied as in the previous analysis, the results shown in figures S9a-i are obtained. Again, the first-shell values for N_{In-O} , R_{In-O} and σ^2_{In-O} are essentially unchanged from previous analyses. There is a dramatic change in the second and third shell fit as a function of k_{max} ; the fit is much more stable with respect to changes in k_{max} and at values of N_{In-In} , R_{In-In} , σ^2_{In-In} , N_{In-In^*} , R_{In-In^*} and $\sigma^2_{In-In^*}$ and more consistent with those expected for *c*-IO. Additionally, the use of both ΔE_0 and $\Delta E_0'$ decreases the reduced X^2 value from 89 when a single ΔE_0 is used for all three shells to 51 when a separate $\Delta E_0'$ is used for the second and third shells.

The values of ΔE_0 and $\Delta E_0'$ will be different from sample to sample as small changes in the experimental procedure will have an effect on the data-model alignment. The relative

positions of ΔE_0 and $\Delta E_0'$, however, should remain the same; that is to say the effect of the first shell on the second and third shells, and, therefore, $\Delta E_0 - \Delta E_0'$ should be a constant. Using the values for the powdered c-IO standard, $\Delta E_0 = 5.4$ eV and $\Delta E_0' = 2.9$ eV, the value of $\Delta E_0'$ will be set to $\Delta E_0 - 2.5$ eV after the value of ΔE_0 is determined by the single-shell model.

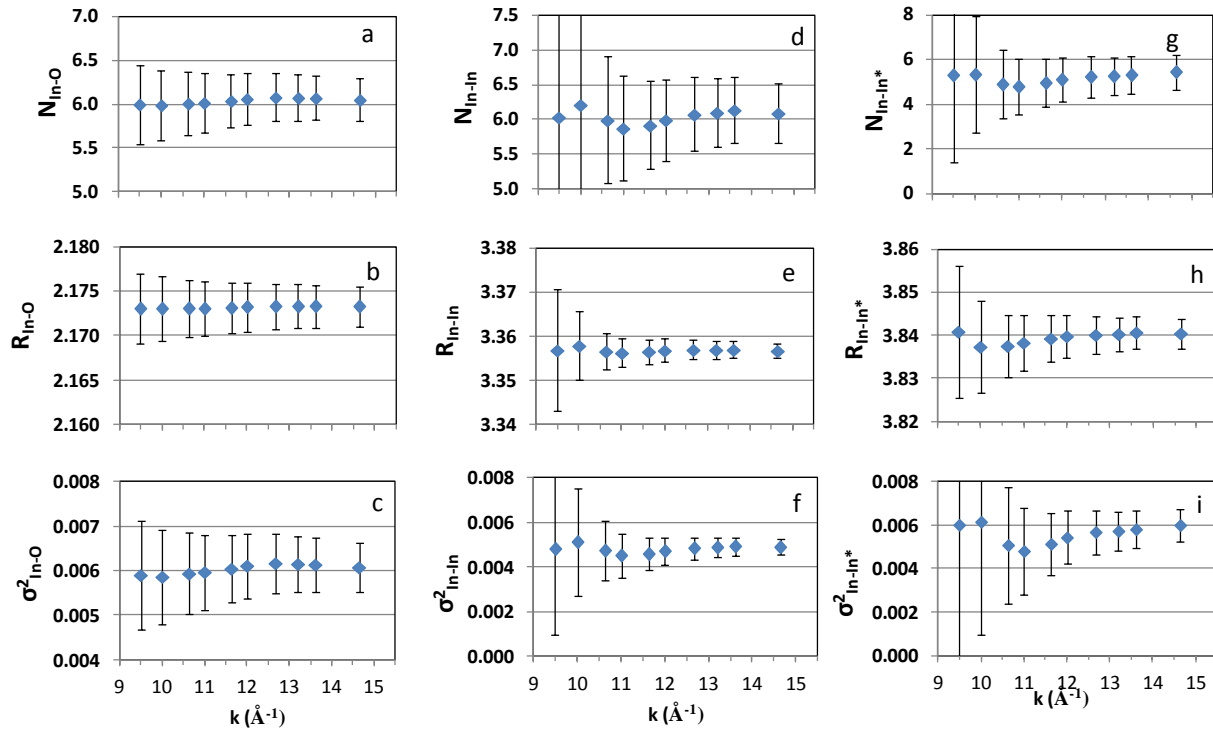


Figure S9: a) N_{In-O} , b) R_{In-O} , c) σ^2_{In-O} , d) N_{In-In} , e) R_{In-In} , f) σ^2_{In-In} , g) N_{In-In^*} , h) R_{In-In^*} , and i) $\sigma^2_{In-In^*}$ for the powder c-IO standard as a function of k_{max} ; $\Delta E_0'$ fit by model as a function of k_{max} .

Third Shell Fitting

The results of the MD simulations can also be used to provide *a priori* knowledge of the of the third shell of the amorphous structure for use in the EXAFS analysis simulations. The average coordination number and statistical spread of bond distances of the third shell for all the cooling rates except 5 K/ps are $N_{In-In^*} \sim 8.2$, $R_{In-In^*} \sim 3.63$ Å and $\sigma^2_{In-In^*} \sim 0.0719$ Å². When the values are set as fixed values into the ARTEMIS program the fit pictured in figure S10 is obtained; the contribution of each shell to the fit is also shown. The contribution of the third shell to the fit is so small that it is barely visible on the scale of the plot as a small hump, smaller than the tail of the first shell contribution centered at ~ 3 Å.

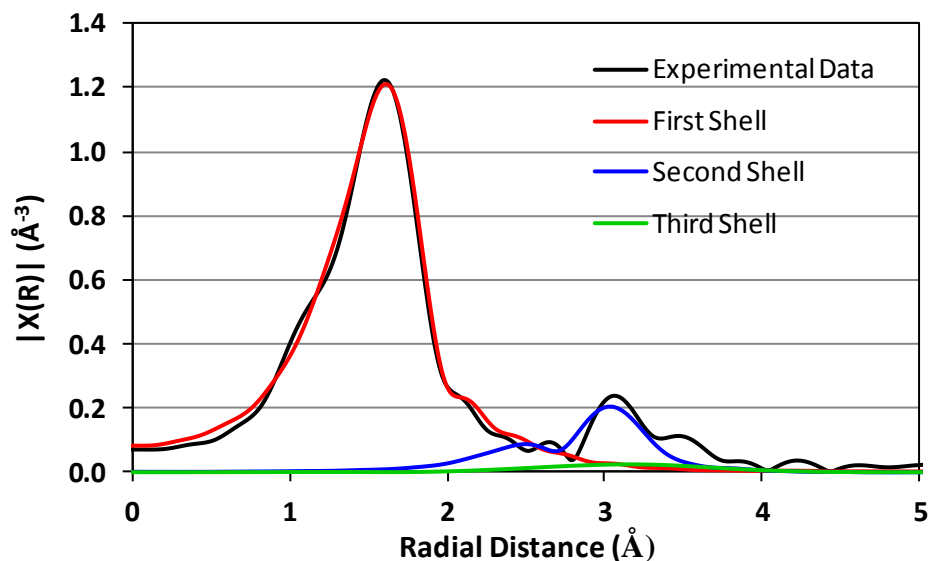


Figure S10: Experiment radial distribution for *a*-IO (black), contribution of first shell (red) contribution of second shell (blue) and contribution of third shell (green); $\sigma^2_{In-In^*} \sim 0.072 \text{ \AA}^2$.

Although the coordination numbers and bond distances have virtually the same meaning between the MD simulations and EXAFS analysis, the statistical spreads are not necessarily the same. Therefore, the first and second shell EXAFS results will be used to “calibrate” the MD simulation results. For the first shell the statistical spread of the bond distances for the amorphous films as derived from the MD-simulations is 0.0110 \AA^2 as compared to $\sim 0.0085 \text{ \AA}^2$ from the EXAFS, a factor of 77%. For the second shell the statistical spread of the bond distances for the amorphous films as derived from the MD-simulations is $\sim 0.020 \text{ \AA}^2$ as compared to $\sim 0.013 \text{ \AA}^2$ from the EXAFS, a factor of 65%. For the third shell an average value of 71% will be used, hence, for constraining the EXAFS model $\sigma^2_{In-In^*} \sim 0.051 \text{ \AA}^2$. Using this lower value of $\sigma^2_{In-In^*}$ in the ARTEMIS program the following fit pictured in figure S11 is obtained; again the contribution of each shell to the fit is also shown. Although the contribution of the third shell is slightly larger it is still minor when compared to the first and second shell. This illustrates nicely that obtaining meaningful results for the third shell of an amorphous sample is not practical.

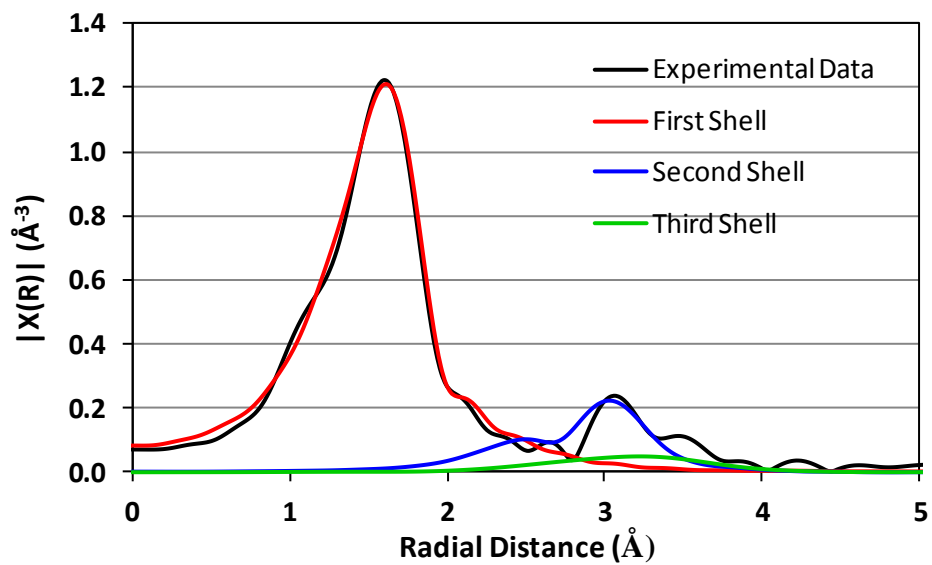


Figure S11: Experiment radial distribution for *a*-IO (black), contribution of first shell (red) contribution of second shell (blue) and contribution of third shell (green); $\sigma^2_{\text{In-In}^*} \sim 0.051 \text{\AA}^2$.

In-O-In angle distribution

Based on the results of the MD simulations for amorphous In-O obtained with different cooling rates, the *In-O-In* angle distribution for corner- and edge-shared *In-In* pairs was calculated, figure S12.

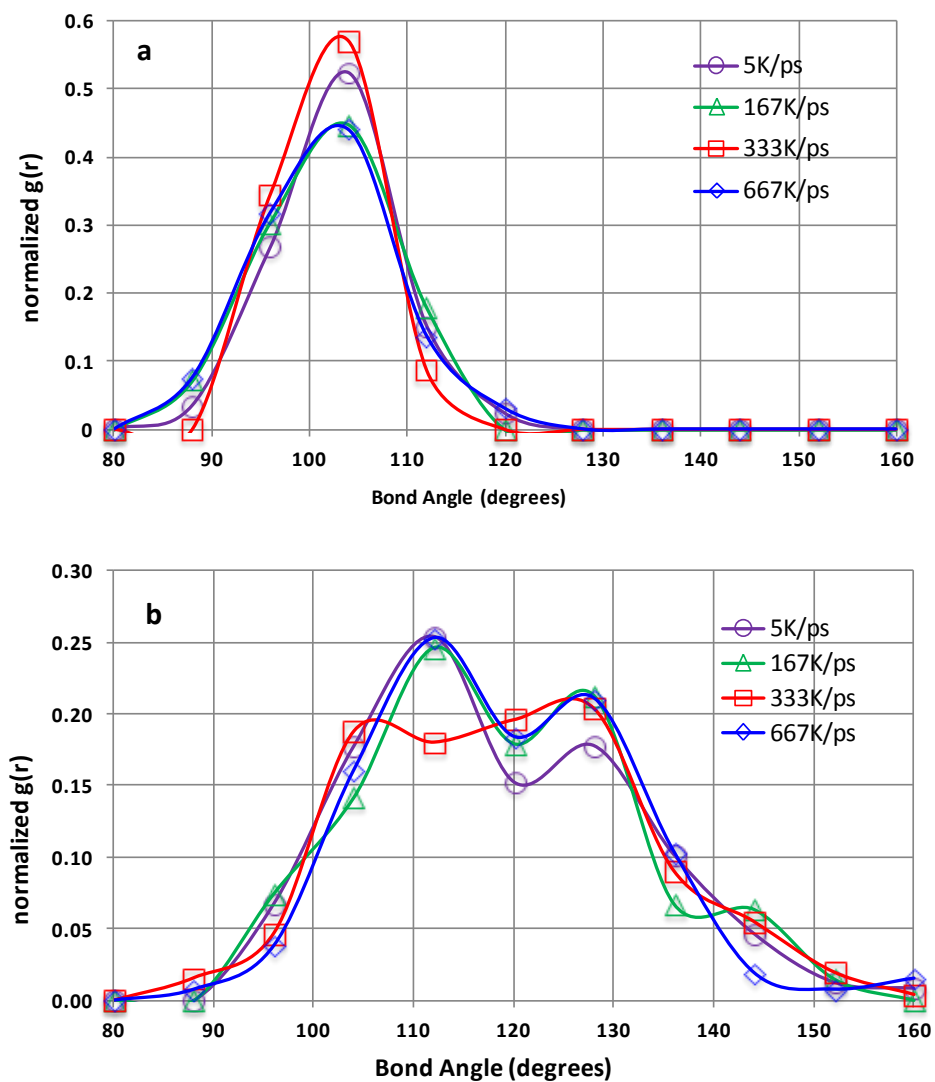


Figure S12: Calculated *In-O-In* bond angle distribution, a) corner shared *In-In* pairs b) edge shared *In-In* pairs.

-
- (1) Proffit, D.E.; Ma, Q.; Buchholz, D.B.; Chang, R.P.H.; Bedzyk, M.J.; Mason, T.O. "Structural and Physical Property Studies of Amorphous Zn-In-Sn-O Thin Films" *J. Am. Ceram. Soc.* **2012**, 95 3657-3664.
 - (2) Hoel, C.A.; Xie, S.; Benmore, C.; Malliakas, C. D.; Gaillard, J.-F.; Poeppelmeier, K.R. "Evidence for Tetrahedral Zinc in Amorphous $\text{In}_{2-2x}\text{Zn}_x\text{Sn}_x\text{O}_3$ (*a*-ZITO)", *Z. Anorg. Allg. Chem.* **2011**, 637, 885-894.
 - (3) Cho, D.-Y.; Jaewon Song, Na, K.D.; Hwang, C.S.; Jeong, J.H.; Jeong, J.K.; Mo, Y.-G. "Local structure and conduction mechanism in amorphous In-Ga-Zn-O films", *Appl. Phys. Lett.* **2009**, 94, 112112-1(3).
 - (4) Nomura, K.; Kamiya, T.; Ohta, H.; Uruga, T.; Hirano, M.; Hosono, H. "Local coordination structure and electronic structure of the large electron mobility amorphous oxide semiconductor In-Ga-Zn-O: Experiment and *ab initio* calculations" *Phys. Rev. B* **2007**, 75, 035212.
 - (5) Yang, D.S.; Lee, J.C.; Chung, J.G.; Lee, E.; Anass, B.; Sung, N.-E.; Lee, J.M.; Kang, H.J.; "Local structure and local conduction paths in amorphous (In,Ga,Hf)-ZnO semiconductor thin films", *Solid States Comm.* **2012**, 152, 1867-1869.
 - (6) Utsuno, F.; Inoue, H.; Shimane, Y.; Shibuya, T.; Yano, K.; Inoue, K.; Hirosawa, I.; Sato, M.; Honma, T. "A structural study of amorphous In_2O_3 films by grazing incidence X-ray scattering (GIXS) with synchrotron radiation", *Thin Solid Films* **2006**, 496, 95-98.
 - (7) T. Moriga, A. Fukushima, Y. Tominari, S. Hosokawa, I. Nakabayashi, K. Tominaga, "Crystallization process of transparent conductive oxides $\text{Zn}_k\text{In}_2\text{O}_{k+3}$ ", *J. Synchrotron Radiat.* **2001**, 8, 785-787.
 - (8) Ravel, B.; Newville, M. "ATHENA, ARTEMIS, HEPHAESTUS: Data analysis for X-ray absorption spectroscopy using IFEFFIT", *J. Synchrotron Radiat.* **2005**, 12, 537-541.
 - (9) Kelly, S. D.; Hesterberg, D.; Ravel, B. "Methods of Soil Analysis. Part 5. Mineralogical Methods" *SSSA Book Series*, no. 5, chapter 14, **2008**, Soil Science Society of America, 677 S. Segoe Road, Madison, WI 53711, USA.